



Gradient-enhanced continuum models of healing in damaged soft tissues

Yiqian He¹ · Di Zuo¹ · Klaus Hackl³ · Haitian Yang¹ · S. Jamaledin Mousavi^{1,2,3} · Stéphane Avril² 

Received: 5 December 2018 / Accepted: 20 April 2019
© Springer-Verlag GmbH Germany, part of Springer Nature 2019

Abstract

Healing of soft biological tissue is the process of self-recovering or self-repairing the injured or damaged extracellular matrix (ECM). Healing is assumed to be stress-driven, with the objective of returning to a homeostatic stress metrics in the tissue after replacing the damaged ECM with new undamaged one. However, based on the existence of intrinsic length scales in soft tissues, it is thought that computational models of healing should be non-local. In the present study, we introduce for the first time two gradient-enhanced constitutive healing models for soft tissues including non-local variables. The first model combines a continuum damage model with a temporally homogenized growth model, where the growth direction is determined according to local principal stress directions. The second one is based on a gradient-enhanced healing model with continuously recoverable damage variable. Both models are implemented in the finite-element package Abaqus by means of a user subroutine UEL. Three two-dimensional situations simulating the healing process of soft tissues are modeled numerically with both models, and their application for simulation of balloon angioplasty is provided by illustrating the change of damage field and geometry in the media layer throughout the healing process.

Keywords Healing · Gradient-enhanced damage · Soft tissue · Growth and remodeling · Abaqus UEL

1 Introduction

Healing of soft biological tissue is the process of self-recovering or self-repairing the injured or damaged extracellular matrix (ECM). Healing is a complex biochemical and biomechanical process, usually divided into four stages: hemostasis, inflammation, proliferation and remodeling. These four stages were described in large details by Comellas et al. (2016) and Cumming et al. (2009). It was reported that the first three stages (from hemostasis to proliferation) may last several weeks, and the final stage of remodeling may last from weeks to years. This last stage consists in a continuous

turnover (synthesis and degradation) of the ECM simultaneously with the production of scar tissue.

Computational modeling can provide insight into healing of soft tissues at both short term and long term. Numerical simulation of healing in soft tissues has been a topic of intense research. Tepole and Kuhl (2013) and Valero et al. (2015) provided a comprehensive review of computational models of dermal wound healing. Generally, there are two types of approaches. The first type focuses on the underlying cellular and biochemical mechanisms based on continuum or hybrid discrete/continuum approaches, including the simulation of wound contraction (Valero et al. 2015; Javierre et al. 2009) and angiogenesis (Schugart et al. 2008). Another type of approaches, more phenomenological, focuses on the change of material properties in the tissue during the remodeling phase.

Important mechanisms involved in soft tissue healing, such as collagen fiber reorientation and collagen turnover, were modeled using growth and remodeling (G&R). A large number of G&R computational approaches exist, among which the constrained mixture theory which was introduced by Humphrey and Rajagopal (2011) about 20 years ago and has been employed by many others (Valentin and Holzapfel

✉ Stéphane Avril
stephane.avril@mines-stetienne.fr

¹ State Key Lab of Structural Analysis for Industrial Equipment, Department of Engineering Mechanics, Dalian University of Technology, Dalian 116024, People's Republic of China

² Mines Saint-Etienne, Univ Lyon, Univ Jean Monnet, INSERM, U1059 SAINBIOSE, 42023 Saint-Étienne, France

³ Mechanik – Materialtheorie, Ruhr-Universität Bochum, Bochum, Germany

2012; Valentín et al. 2013; Famaey et al. 2018). The computational cost of this approach was significantly reduced by a temporally homogenized technique proposed by Cyron et al. (2016).

Recently, Comellas et al. (2016) developed a homeostasis-driven turnover remodeling model for healing in soft tissues based on continuum damage mechanics (CDM). In this approach, the healing process was simulated by a continuously recoverable damage variable (Comellas et al. 2016).

Intrinsic length scales, such as the length of collagen fibers, are physically inherent to soft tissues and numerical models of healing should consider them through non-local approaches. Moreover, mesh dependency is a traditional issue in damage models that non-local approaches are able to overcome (Dimitrijevic and Hackl 2008; Dimitrijevic and Hackl 2011; Waffenschmidt et al. 2014). However, there are no non-local computational models for soft biological tissues in the literature to the authors' best knowledge, and the effects of intrinsic length scales in healing are still unknown.

From the viewpoint of continuum damage mechanics, local continuum damage models have a major drawback: their solutions are significantly mesh-dependent, with vanishing of the localized damage zone when the mesh is refined (Waffenschmidt et al. 2014; Mousavi et al. 2018).

First, non-local damage models of soft tissues were introduced by Waffenschmidt et al. (2014), using a gradient-enhanced large-deformation continuum damage model based on the previous work of Dimitrijevic and Hackl (2008, 2011). In this approach, the local free energy function is enhanced by a gradient-term containing the gradient of an additional non-local damage variable, and a penalization term is also introduced to ensure equivalence between the local and non-local damage variables. Ferreira et al. (2017) also presented an integral-type non-local averaging damage model for anisotropic hyperelastic materials. Despite this state of the art in non-local damage modeling, healing of soft tissues remains a frontier in non-local continuum mechanics. Fernández et al. (2012) proposed a remodeling model for the bone tissue including a diffusion term to address localization problems.

In this paper, we introduce for the first time two gradient-enhanced constitutive healing models for soft tissues including non-local variables in a similar fashion as in previous work from Dimitrijevic and Hackl (2008, 2011) and Waffenschmidt et al. (2014). By virtue of the proposed model, an intrinsic length-scale parameter is for the first time included in a healing model with a gradient-enhanced term, and a non-local variable is introduced with a penalization term to reduce mesh dependency.

The first non-local healing model combines the non-local continuum damage model with a temporally homogenized G&R model. Damage is modeled with the gradient-enhanced approach, and a term of mass production is introduced to

model mass variations due to tissue production. There exist a variety of growth models, from surface to volume growth, taking into account mass variations in biological materials as described in Ganghoffer and Haussy (2005), Ganghoffer (2010a, b, 2012), Ganghoffer and Boubaker (2017). In this work, a temporally homogenized growth model is used based on the work from Cyron et al. (2016), permitting significant reduction of the computational cost compared to original work from Humphrey and Rajagopal (2011). In this temporally homogenized growth model, the rate of mass production satisfies a homeostasis-driven governing equation. Mass production induces inelastic deformations which are modeled in a similar fashion as in plasticity (Rodriguez et al. 1994). We assume that the growth direction is aligned with the direction of the first principal stress.

The second non-local healing model is based on the healing model proposed by Comellas et al. (2016) that we turned into a gradient-enhanced version. In this model, the healing is simulated by turning the damage variable into a recoverable variable. The process of damage recovery is controlled by the healing rate and can be integrated numerically by a finite difference scheme.

Both models are implemented in the finite-element package Abaqus by means of a user subroutine UEL. In the following, the general gradient-enhanced G&R healing model is developed in Sect. 2. Section 3 provides two specific gradient-enhanced healing models, including the details of equations for the rate and direction of growth and the evolution of damage. Section 4 outlines the process of numerical implementation of the proposed methods. Three examples are illustrated in Sect. 5 with the aim of verifying these models. Finally, conclusions are given in Sect. 6.

2 General equations for gradient-enhanced healing models

2.1 Basic kinematics

Let $\mathbf{x} = \boldsymbol{\varphi}(\mathbf{X}, t)$ describe deformations of a body from referential positions $\mathbf{X} \in \kappa(0)$ to their actual counterparts $\mathbf{x} \in \kappa(t)$. Within this framework, the deformation gradient is defined as

$$\mathbf{F} = \nabla_{\mathbf{x}} \boldsymbol{\varphi} \quad (1)$$

Accordingly, reference volumes dV and current volumes $d\nu$ are related such as

$$d\nu = \det(\mathbf{F})dV = JdV \quad (2)$$

where J is the Jacobian of the deformation (determinant of \mathbf{F}).

Growth is a process of mass production or removal, whereby volumes may change inelastically. This is captured

by an inelastic deformation gradient \mathbf{F}_g . Therefore, the total deformation at any time t is

$$\mathbf{F}(t) = \mathbf{F}_e(t) \mathbf{F}_g(t) \tag{3}$$

2.2 Gradient-enhanced healing model

The general strain energy function per unit reference volume at each G&R time t is assumed as

$$\psi(t) = H(t) \hat{\psi}(\mathbf{F}^e(t)) \tag{4}$$

where $\hat{\psi}(\mathbf{F}^e(t))$ is the original (undamaged) strain energy depending on the elastic deformation $\mathbf{F}_e(t)$, $H(t)$ is a time-dependent function to describe the level of healing and has different forms for different healing models in the following section.

Following the approach of Dimitrijevic and Hackl (2008, 2011), a gradient-enhanced non-local free energy function is added to the energy given in Eq. (4),

$$\psi(t) = H(t) \hat{\psi}(\mathbf{F}^e(t)) + \frac{c_d}{2} \|\nabla_{\mathbf{x}} \phi\|^2 + \frac{\beta_d}{2} [\phi - \gamma_d d]^2 \tag{5}$$

In Eq. (5), c_d represents the gradient parameter that defines the degree of gradient regularization and the internal length scale. Comparing Eqs. (4) and (5), two additional terms are added, introducing the three following variables:

- the variable field ϕ , which transfers the values of the damage parameter across the element boundaries to make it non-local in nature,
- the energy-related penalty parameter β_d which approximately enforces the local damage field and the non-local field to coincide,
- parameter γ_d which is used as a switch between the local and enhanced model.

3 Two gradient-enhanced healing models

3.1 Gradient-enhanced healing model based on G&R

In this section, a new gradient-enhanced healing model based on G&R is presented inspired by Valentín et al. (2013). The strain energy function per unit reference volume at each G&R time t is assumed as

$$\psi_1(t) = H_1(t) \cdot \hat{\psi}(\mathbf{F}^e(t)) + \frac{c_d}{2} \|\nabla_{\mathbf{x}} \phi\|^2 + \frac{\beta_d}{2} [\phi - \gamma_d d]^2 \tag{6}$$

where

$$H_1(t) = f(d) \frac{\rho_0}{\rho(t)} Q(t) + \frac{\rho_g(t)}{\rho(t)} \tag{7}$$

In Eqs. (7) ρ_0 is mass density per unit reference volume at $t = 0$, just prior to the beginning of G&R, $\rho_g(t)$ denotes the change of mass density computed by $\rho_g(t) = \rho(t) - \rho_0$, and $\rho_g(t)$ are caused by G&R only and induce inelastic deformations, whereas the motion induces elastic motions. $Q(t) \in [0, 1]$ is the mass fraction that was present at $t = 0$ that survives to time t (Valentín et al. 2013) and $f(d)$ represents a function of damage variable d that measures the material stiffness loss and satisfies the conditions.

$$f(d) : \mathfrak{R}^+ \rightarrow (0, 1] \left\{ f(0) = 1, \lim_{d \rightarrow \infty} f(d) = 0 \right\} \text{ with } f(d) \in [0, 1] \tag{8}$$

It is noted that density variations $\rho_g(t)$ are caused by G&R and induce inelastic deformations, whereas the elastic deformation gradient $\mathbf{F}_e(t)$ satisfies Eqs. (3) and (4).

According to Braeu et al. (2017), the deformation caused by growth is regarded as an inelastic deformation, where the change of volume is related to a change in mass. Hence, the rate of inelastic deformation gradient $\dot{\mathbf{F}}_g$ is obtained as in Braeu et al. (2017)

$$\dot{\mathbf{F}}_g = \frac{\dot{\rho}(t)}{\rho(0) \left| \mathbf{F}_g \right| \left[(\mathbf{F}_g)^{-T} : \mathbf{B} \right]} \mathbf{B} \tag{9}$$

where the second-order tensor \mathbf{B} defines the growth direction and is normalized without loss of generality such that $\text{tr}(\mathbf{B}) = 1$.

The Davis’ law (Davis 1867) suggests that perturbations from a preferred homeostatic state in soft collagenous tissues are answered by biological G&R processes aimed to restore normalcy. The Davis’s law can be invoked to justify anisotropic growth, as adding mass in directions normal to the maximum principal stress will automatically reduce the stress value and make it converge back to the homeostatic value (Menzel 2005; Cyron and Humphrey 2017). A very good case illustrating this effect is related to the thickening of arteries due to hypertension. Indeed, many observations showed that arteries tend to thicken in response to sustained increases in blood pressure (i.e., hypertension) (Sáez et al. 2014). Hence, we assume the growth direction is aligned with the direction of the first principal stress. For instance, in two-dimensional cases, if θ_p is the orientation of the first principal stress, the growth direction tensor \mathbf{B} in Eq. (9) can be expressed as

$$\mathbf{B} = \begin{bmatrix} \cos^2 \theta_p & 0 \\ 0 & \sin^2 \theta_p \end{bmatrix} \tag{10}$$

To determine the rate of mass production caused by growth $\dot{\rho}_g(t)$ in Eq. (7), two models are considered in this paper:

3.1.1 G&R constant model

In the *G&R constant model*, the mass production is assumed to be constant during the healing process as

$$k_g \cdot \rho_0 \cdot Q(t) + \rho_g(t) = \text{const} \tag{11}$$

where k_g is the healing fraction to denote the percentage of mass before the healing to participate to mass balance.

Therefore, the $\dot{\rho}_g(t)$ is obtained by computing the time derivative such as

$$\dot{\rho}_g(t) = -k_g \cdot \rho_0 \cdot \dot{Q}(t) \tag{12}$$

Considering total mass density $\rho(t) = \rho_0 + \rho_g(t)$, so the rate of total mass density is

$$\dot{\rho}(t) = (1 - k_g)\rho_0 \cdot \dot{Q}(t) \tag{13}$$

The total mass density $\rho(t)$ at time step $n + 1$ can be obtained by the finite difference scheme

$$\rho(t_{n+1}) = (1 - k_g)\rho_0 \cdot \dot{Q}(t_n) \cdot \Delta t + \rho(t_n) \tag{14}$$

where Δt is the time step.

According to Eqs. (11) and (14), the mass densities $\rho_g(t)$ and $\rho(t)$ in Eq. (7) are determined.

3.1.2 G&R homeostatic model

In the *G&R homeostatic model*, the rate of mass production is mediated by the current stress as proposed by Braeu et al. (2017).

$$\dot{\rho}_g(t) = \rho_g(t) \mathbf{K}_\sigma : (\boldsymbol{\sigma}_R - \boldsymbol{\sigma}_h) + \dot{D}(t) \tag{15}$$

where \mathbf{K}_σ is a gain-type second-order tensor, for two-dimensional case, it is assumed that

$$\mathbf{K}_\sigma = \begin{bmatrix} k_\sigma & 0 \\ 0 & k_\sigma \end{bmatrix} \tag{16}$$

and $\dot{D}(t)$ is a generic rate function for additional deposition that is not stress mediated (describing additional deposition or damage processes affecting the net mass production driven by other factors such as chemical degradation and/or mechanical fatigue processes), $\boldsymbol{\sigma}_R = \mathbf{R}^T \boldsymbol{\sigma} \mathbf{R}$ is the co-rotated Cauchy stress tensor with the orthonormal rotation tensor \mathbf{R} in polar decomposition and $\boldsymbol{\sigma}_h$ denotes the homeostatic stress.

The mass production $\rho_g(t)$ at time step $n + 1$ can be obtained by the finite difference scheme in the absence of $\dot{D}(t)$ for simplicity

$$\rho_g(t_{n+1}) = (\rho_g(t_n) \mathbf{K}_\sigma : (\boldsymbol{\sigma}_R - \boldsymbol{\sigma}_h)) \cdot \Delta t + \rho_g(t_n) \tag{17}$$

Accordingly, total mass density $\rho(t)$ at time step $n + 1$ can be obtained by the finite difference scheme

$$\rho(t_{n+1}) = (\rho_g(t_n) \mathbf{K}_\sigma : (\boldsymbol{\sigma}_R - \boldsymbol{\sigma}_h)) \cdot \Delta t + \rho_g(t_n) + \rho_0 \cdot Q(t_{n+1}) \tag{18}$$

3.2 Non-local Comellas model

In this section, another gradient-enhanced healing model is established based on the healing model proposed by Comellas et al. (2016), in which the effective damage D_{eff} is assumed as a recoverable variable in the process of healing. In this paper, we apply similar constitutive equations into a gradient-enhanced framework. Here only some key equations for healing process are written, the readers can refer to literature (Dimitrijevic and Hackl 2008, 2011; Waffenschmidt et al. 2014) for detailed equations.

The strain energy function per unit reference volume is written such as

$$\psi_2(t) = H_2(t) \cdot \hat{\psi}(\mathbf{F}_e(t)) + \frac{c_d}{2} \|\nabla_{\mathbf{x}} \phi\|^2 + \frac{\beta_d}{2} [\phi - \gamma_d d]^2 \tag{19}$$

where

$$H_2(t) = 1 - D_{\text{eff}}(t) \tag{20}$$

In Eq. (19), the second term is to introduce the gradient parameter c_d that defines the degree of gradient regularization and the internal length scale. In order to make the model non-local, the third term is used for penalizing the difference between the damage field d and the non-local variable field ϕ .

According to Comellas et al. (2016), the effective damage D_{eff} is assumed to a recoverable variable, and its rate

$$\dot{D}_{\text{eff}} = \dot{D} - \dot{R} \tag{21}$$

where \dot{D} is the rate of explicit Kachanov-like mechanical damage variable $D = f(d)$ and \dot{R} is the healing rate given as

$$\dot{R} = \dot{\eta} \langle D_{\text{eff}} - \xi \rangle \tag{22}$$

where $\langle \cdot \rangle$ represents the Macaulay brackets, η is a function that regulates how fast healing occurs and ξ defines the percentage of stiffness that is not recovered at the end of the healing process.

The effective damage at time step $n + 1$ can be obtained by the finite difference scheme proposed by Comellas et al. (Comellas et al. 2016) as

$$D_{\text{eff}}^{n+1} = (D_{\text{eff}}^n + \Delta D + \dot{\eta} \xi \Delta t) / (1 + \dot{\eta} \Delta t) \tag{23}$$

3.3 Total potential energy and variational formulation

The potential energy can be written as (Dimitrijevic and Hackl 2008; Dimitrijevic and Hackl 2011)

$$\Pi = \int_{\Omega} \psi dV - \int_{\Omega} \bar{\mathbf{B}} \cdot \boldsymbol{\varphi} dV - \int_{\partial\Omega} \bar{\mathbf{T}} \cdot \boldsymbol{\varphi} dV \tag{24}$$

where $\bar{\mathbf{B}}$ denotes the body force vector per unit reference volume and $\bar{\mathbf{T}}$ characterizes the traction vector per unit reference surface area, Ω represents the reference volume and $\partial\Omega$ is the surface boundary of Ω .

Minimization of the potential energy with respect to the primal variables $\boldsymbol{\varphi}$ and ϕ results in a system of equations that have to be zeroed globally

$$\int_{\Omega} \mathbf{P} : \nabla_{\mathbf{X}} \delta \boldsymbol{\varphi} dV - \int_{\Omega} \bar{\mathbf{B}} \cdot \delta \boldsymbol{\varphi} dV - \int_{\partial\Omega} \bar{\mathbf{T}} \cdot \delta \boldsymbol{\varphi} dV = 0 \tag{25}$$

$$\int_{\Omega} \mathbf{Y} : \nabla_{\mathbf{X}} \delta \phi dV - \int_{\Omega} Y \delta \phi dV = 0 \tag{26}$$

where $\bar{\mathbf{B}}$ is the body force vector and \mathbf{P} the first Piola–Kirchhoff stress tensor.

The vectorial damage quantity \mathbf{Y} and the scalar damage quantity Y are defined such as

$$\mathbf{P} = \partial_{F_e} \psi, \quad \mathbf{Y} = \partial_{\nabla_{\mathbf{x}} \phi} \psi, \quad Y = \partial_{\phi} \psi \tag{27}$$

Accordingly, the spatial quantities are given by

$$\boldsymbol{\sigma} = \mathbf{P} \cdot \text{cof}(\mathbf{F}^{-1}), \quad y = \mathbf{Y} \cdot \text{cof}(\mathbf{F}^{-1}), \quad y = \mathbf{J}^{-1} Y \tag{28}$$

where the factor defined as $\text{cof}(\mathbf{F}) = \mathbf{J} \mathbf{F}^{-t}$.

3.4 Damage evolution

The evolution of the damage variable d can be found in the works by Dimitrijevic and Hackl (2008, 2011) and Waffenschmidt et al. (2014); here, only some key equations are outlined.

Following standard thermodynamic consideration of Dimitrijevic and Hackl (2008, 2011), damage conjugate q is defined as

$$q = - \frac{\partial \psi}{\partial d} \tag{29}$$

The damage condition at any time of the loading process is based on an energy-release rate threshold condition and corresponds to the model of Simo and Ju (1987)

$$\Phi_d = q - r_1 \leq 0 \tag{30}$$

Based on the postulate of maximum dissipation, the differential equation of the evolution of damage variable is subjected to Kuhn–Tucker optimality conditions (Dimitrijevic and Hackl 2008, 2011)

$$\dot{d} = \dot{\kappa} \frac{\partial \Phi_d}{\partial q}; \quad \dot{\kappa} \geq 0, \quad \Phi_d \leq 0, \quad \dot{\kappa} \Phi_d = 0 \tag{31}$$

4 Finite-element discretization

In order to approach the process of replacing the damaged soft tissue with new undamaged, FE computation is also divided into two stages, i.e., the damage process and the healing process. This section only derives the implementation of FE for the healing process. For the detailed process of FE computation process, the readers can refer the work by Waffenschmidt et al. (2014).

Following the works of Dimitrijevic and Hackl (2008, 2011) and Waffenschmidt et al. (2014), a quadratic serendipity interpolation is used for both the geometry \mathbf{X} and the field variables $\boldsymbol{\varphi}$, and a bilinear interpolation is used for the non-local field ϕ . According to the isoparametric concept, these interpolations are written as

$$\mathbf{X}^h = \sum_{I=1}^{n_{en}^{\varphi}} N_I(\xi) \mathbf{X}_I, \quad \boldsymbol{\varphi}^h = \sum_{I=1}^{n_{en}^{\varphi}} N_I(\xi) \boldsymbol{\varphi}_I, \quad \phi^h = \sum_{I=1}^{n_{en}^{\phi}} N_I(\xi) \phi_I \tag{32}$$

where ξ denotes the coordinates in the reference element, n_{en}^{φ} and n_{en}^{ϕ} are the displacement nodes and non-local damage nodes per element, respectively.

For the healing process, at a loading time t , an incremental scheme based on Newton’s method is applied (Dimitrijevic and Hackl 2008, 2011)

$$\begin{bmatrix} \mathbf{R}_{\boldsymbol{\varphi}} \\ \mathbf{R}_{\phi} \end{bmatrix}^i + \begin{bmatrix} \mathbf{K}_{\boldsymbol{\varphi}\boldsymbol{\varphi}} & \mathbf{K}_{\boldsymbol{\varphi}\phi} \\ \mathbf{K}_{\phi\boldsymbol{\varphi}} & \mathbf{K}_{\phi\phi} \end{bmatrix} \cdot \begin{bmatrix} \Delta \boldsymbol{\varphi} \\ \Delta \phi \end{bmatrix}^{i+1} = \begin{bmatrix} \mathbf{0} \\ \mathbf{0} \end{bmatrix} \tag{33}$$

where

$$\mathbf{K}_{\boldsymbol{\varphi}\boldsymbol{\varphi}} = \int_{\Omega} \nabla_{\mathbf{x}}^T N \cdot [\mathbf{C}_h(t)] \cdot \nabla_{\mathbf{x}} N \, dv + \int_{\Omega} [\nabla_{\mathbf{x}}^T N \cdot \boldsymbol{\sigma} \cdot \nabla_{\mathbf{x}} N] \mathbf{I} \, dv \tag{34}$$

$$\mathbf{K}_{\boldsymbol{\varphi}\phi} = \int_{\Omega} \nabla_{\mathbf{x}}^T N \cdot \frac{d\boldsymbol{\sigma}}{d\phi} \cdot N \, dv \tag{35}$$

$$\mathbf{K}_{\phi\boldsymbol{\varphi}} = \int_{\Omega} N^T \cdot 2 \frac{dy}{d\mathbf{g}} \cdot \nabla_{\mathbf{x}}^T N \, dv \tag{36}$$

$$\mathbf{K}_{\phi\phi} = \int_{\Omega} N^T \cdot \frac{dy}{d\phi} \cdot N \, dv + \int_{\Omega} \nabla_{\mathbf{x}}^T N \cdot \frac{dy}{d\phi} \cdot \nabla_{\mathbf{x}}^T N \, dv \tag{37}$$

In the above equations, the tangent terms $d\boldsymbol{\sigma}/d\phi, 2dy/d\mathbf{g}, dy/d\phi$ and $dy/d\phi$ are the same with the damage process as in the work by Waffenschmidt et al. (2014), $\mathbf{C}_h(t)$ is a new time-dependent tangent stress–strain matrix in the damage and healing process given as

$$\mathbf{C}_h(t) = H(t) \cdot \mathbf{C}_e \tag{38}$$

where the \mathbf{C}_e is the elasticity tensors for undamaged material, $H(t)$ defined in Eq. (6) is to describe the level of healing

and has different forms for the non-local G&R healing model and the non-local Comellas model as introduced in the following section.

4.1 G&R healing model with gradient-enhanced damage

For the non-local G&R healing models, the form of $H(t)$ is determined by the choice of model for mass production.

If the *G&R constant model* with finite difference scheme in the time domain is used, $H(t)$ at the $(n + 1)$ th time step by substituting Eqs. (12) and (14) into Eq. (7)

$$H(t_{n+1}) = \frac{\rho_0}{\rho(t_{n+1})} f(d) Q(t_{n+1}) + \frac{(1 - k_g) \rho_0 \cdot \dot{Q}(t_n) \cdot \Delta t + \rho_g(t_n)}{\rho(t_{n+1})} \tag{39}$$

If the *G&R homeostatic model* with finite difference scheme in time domain is obtained by substituting Eqs. (15) and (18) into Eq. (7)

$$H(t_{n+1}) = \frac{\rho_0}{\rho(t_{n+1})} f(d) Q(t_{n+1}) + \frac{(\rho_g(t_n) \mathbf{K}_\sigma : (\boldsymbol{\sigma}_R - \boldsymbol{\sigma}_h)) \cdot \Delta t + \rho_g(t_n) + \rho_0 \cdot Q(t_{n+1}))}{\rho(t_{n+1})} \tag{40}$$

The elastic deformation is obtained from Eq. (32), and the inelastic deformation due to G&R from Eq. (9); finally, the total deformation is given by

$$\mathbf{F}(t_{n+1}) = \nabla_{\mathbf{X}} \boldsymbol{\varphi}(t_{n+1}) \cdot \mathbf{F}_g(t_{n+1}) \tag{41}$$

In Eq. (41), the first factor on the right-hand side $\nabla_{\mathbf{X}} \boldsymbol{\varphi}(t_{n+1})$ refers to the elastic deformation, and the left-hand side $\mathbf{F}(t_{n+1})$ is the total deformation gradient.

4.2 Non-local Comellas model

For the non-local Comellas model,

$$H(t_{n+1}) = 1 - (D_{eff}(t_n)) + \Delta D + \eta \xi \Delta t / (1 + \eta \Delta t) \tag{42}$$

Since the deformation due to growth is not considered in non-local Comellas model, the total deformation is given without $\mathbf{F}_g(t_{n+1})$ by

$$\mathbf{F}(t_{n+1}) = \nabla_{\mathbf{X}} \boldsymbol{\varphi}(t_{n+1}) \tag{43}$$

The process of numerical implementation is provided in Table 1. Examples for these expressions are given in the following sections for specific applications.

5 Numerical examples

The gradient-enhanced model and the different healing models were incorporated within the commercial finite-element software Abaqus/Standard by means of a user element

subroutine (UEL) and the 2D examples are solved as plane strain problems. They were applied in three different situations described in the following subsections. In all of them a simple damage function $f(d) = e^{-d}$ is used.

5.1 Uniaxial tension

A square plate with 1 cm edge length is subjected to a displacement-driven pure tensile load as shown in Fig. 1. The neo-Hookean hyperelastic and damage material properties are reported in Table 2. Assume that the healing process is beginning from time $t = 100$ days, and $Q(t') = e^{-\eta t'}$ with $t' = t - 100$, where parameter η_t describes the speed of mass degradation. According to (Comellas et al. 2016), a relatively large bulk modulus is chosen compared with the shear modulus.

5.1.1 G&R constant model

The performance of *G&R constant model* is firstly tested by calculating the variation of average Cauchy stress along the right side of plate with time as shown in Fig. 2. Figure 2a shows the influence of the degradation speed parameter η_t in the *G&R constant model*, where a larger η_t causes a higher stress, meaning that a faster degradation (mass decrease) leads to a higher level of healing. Figure 2b investigates the influence of the healing fraction k_g . The following values are tested: $k_g = 0.8, 1.0$ and 1.5 , respectively. Firstly, the *G&R constant model* simulates the increase in stress in the process of healing. Secondly, low k_g values cause higher stress, as both $k_g < 1$ and $\dot{Q}(t) < 0$ will lead $\dot{\rho}(s) < 0$ according to Eq. (13), so a smaller inelastic deformation \mathbf{F}_g is produced in Eq. (9), and as a constant total displacement loading is applied, a larger elastic deformation \mathbf{F}_e is obtained in Eq. (3), and finally, the obtained stress is higher than the one with $k_g \geq 1$.

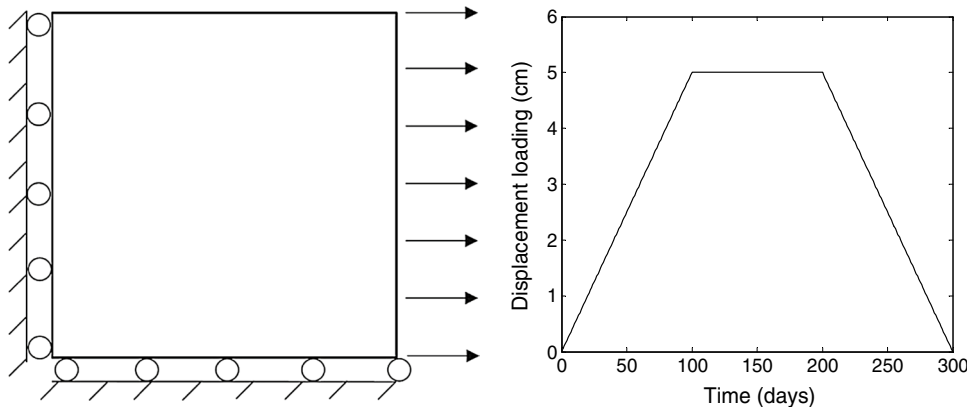
5.1.2 G&R homeostatic model

Figure 2c, d illustrates the stress curves for the *G&R homeostatic model*, where the influence of the homeostatic stress value $\boldsymbol{\sigma}_h$ and of the gain parameter k_σ is shown in Fig. 2c, d, respectively. Considering that the homeostatic stress was consistent with stresses commonly applied to soft tissues in vivo (Simo and Ju 1987; Humphrey et al. 2014), here we

Table 1 Different steps of the numerical implementation at the Gauss point level for gradient-enhanced continuum healing models

0. Initialization at $t=0$ and $n=0$
Mechanical damage $d^n = 0$ and healing function $H^n = 1$
1. Algorithm at each load increment n
1.1 Given: Total deformation gradient tensor \mathbf{F} , elastic deformation \mathbf{F}_e , inelastic deformation \mathbf{F}_g and material properties
1.2 Compute driving force from Equation (29)
1.3 Check damage condition from Equation (30), if $\Phi_d = q - r_1 \leq 0$ go to 1.5, else go to 1.4
1.4 Update damage $d^{n+1} = d^n + \Delta d$ from Equation (31)
1.5 Update healing function H^{n+1} IF (G&R constant model) Compute H^{n+1} from Equation (39) IF (G&R homeostatic model) Compute H^{n+1} from Equation (40) IF (Non-local Comellas model) Compute H^{n+1} from Equation (42)
1.6 Compute the stress state for the present step σ
1.7 Compute tangent moduli $d\sigma/d\phi$, $2dy/dg$, $dy/d\phi$ and $dy/d\phi$ in Equations (34-37).

Fig. 1 Geometry and displacement applied for the uniaxial tension case study



set the values of homeostatic stresses lower than the maximum stress reached after damage, so that G&R worked at reducing this stress in order to converge toward the homeostatic stress, consequently inducing healing. The results show the convergence of the stress toward the homeostatic stress after healing for all the tested cases. A larger gain

parameter k_σ results in a faster convergence. Furthermore, the sensitivity of the size of time step Δt is reported in Fig. 2e, and the results show that different Δt values have no significant influence on the convergence toward the homeostatic state.

Table 2 Hyperelastic, damage and healing parameters used in the homogeneous uniaxial tensile test example

Type	Description	Symbol	Values	Units
Hyperelastic	Shear modulus	μ_e	1.5	MPa
	Bulk modulus	κ_e	75.0	MPa
Damage	Saturation parameter	η_d	1.0	MPa ⁻¹
	Damage threshold	κ_d	8.0	MPa
Healing	G&R constant model	k_g	[0.8, 1.0, 1.5]	–
		η_r	[0.001, 0.005, 0.01]	–
	G&R homeostatic model	k_σ	[0.005, 0.01, 0.02]	–
		η_r	0.01	–
	Non-local Comellas model	$\dot{\eta}$	0.01	Days ⁻¹
	ξ	0.0	–	

5.1.3 Comparison of the G&R models with the non-local Comellas model

The *G&R constant model*, the *G&R homeostatic model* and the *non-local Comellas model* are compared in Fig. 3. It is shown that both the *G&R constant model* and the *G&R homeostatic model* yield a nonzero stress as the displacement loading is entirely unloaded as shown in Fig. 3a. Accordingly, the temporal variations of elastic and inelastic deformations are shown in Fig. 3b, in which nonzero inelastic deformations obtained in the *G&R constant model* and the *G&R homeostatic model* are shown. Comparatively, there is no inelastic deformation for the *non-local Comellas model*.

5.2 Open-hole plate

The second numerical example is a rectangular plate with a hole, loaded under displacement-driven conditions. The geometry and the loading curves are shown in Fig. 4. The neo-Hookean hyperelastic and damage material properties are reported in Table 3. Due to the symmetry, only a quarter of the plate is analyzed. For the material parameters, as in Example 1, a relatively large bulk modulus is chosen compared with the shear modulus (Comellas et al. 2016).

5.2.1 G&R constant model

The stress curves shown in Fig. 12a prove the mesh independence for the *G&R constant model*. The evolution of the time-dependent damage function $H(t)$ is shown throughout the healing process in Fig. 5 for two different mesh sizes. Again, the results are fully mesh independent.

The influence of non-local effects of the *G&R constant model* is investigated in Fig. 6 with different c_d values. c_d is the parameter representing the effect of internal length scales, or more specifically as the parameter related to the

average length of microstructural components in the soft tissues. The results show that a higher c_d leads to smaller damage and a narrower damage zone during both the damage and healing process. This can be explained by the larger width of the ‘activated zone’ in case of higher c_d in the model (Dimitrijevic and Hackl 2008, 2011); hence, the changes in the damage variable will affect a larger region, which is related to larger internal length scales of the soft tissue.

5.2.2 G&R homeostatic model

For the *G&R homeostatic model*, the stress curves and the evolution of damage distribution with time are shown in Figs. 12b and 7, respectively, again revealing a very good mesh independence, the homeostatic stress is set to a value of 0.000815 MPa for the average Cauchy stress at the right side of plate, which represents stress at time $t = 40$ days. Unlike the previous results obtained with the *G&R constant model*, the stress decreases and tends to converge toward a target value during healing, which represents the homeostatic state.

The influence of non-local effects in the *G&R homeostatic model* is also investigated in Fig. 8. The effect of internal length scales is shown with different c_d values. The decrease in the damage region is shown during healing with a larger value of c_d .

Figure 9 illustrates the influence of values of homeostatic stress and the level of damage, respectively. In Fig. 9a, the results show good convergence to the state of homeostatic stress for healing with three different prescribed σ_h . Moreover, the ability of the *G&R homeostatic model* to simulate different levels of damage/healing is analyzed by varying the penalty parameter β_d in the non-local damage model as shown in Fig. 9b. It is shown that although the *G&R homeostatic model* is capable of simulating the process of convergence of stress to the homeostatic state for $\beta_d = 0.004$ and $\beta_d = 0.006$, a simulation failure occurs for $\beta_d = 0.002$ with more damage contained. The reason of computational failure could be that a more severe damage causes a more

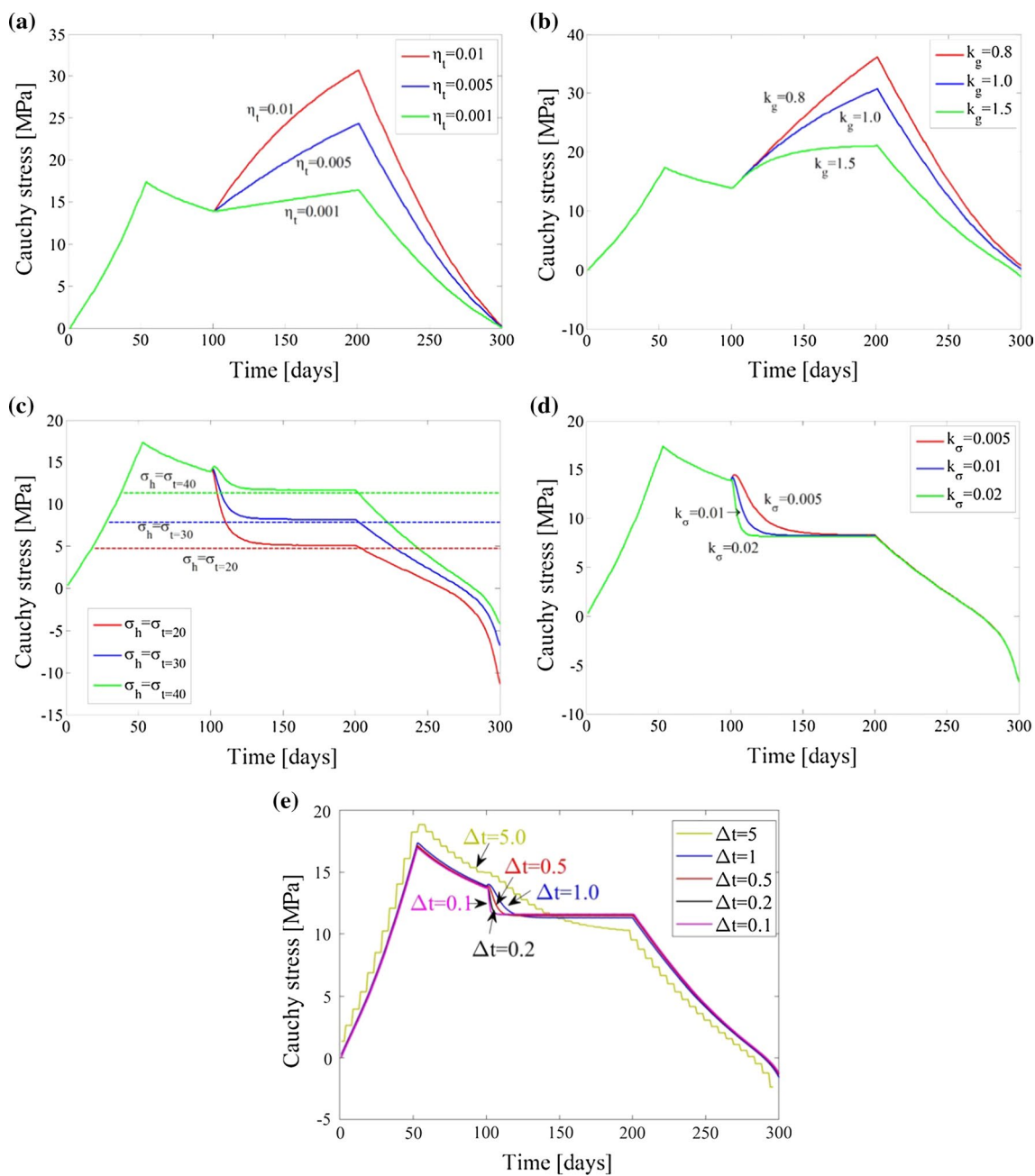


Fig. 2 Stress curves obtained in the homogeneous uniaxial tension example. **a** Influence of the degradation speed parameter η_t for G&R constant model. **b** Influence of the healing parameter k_g for G&R constant model. **c** Influence of the homeostatic

stress σ_h for G&R homeostatic model. **d** Influence of the gain parameter k_σ for G&R homeostatic model. **e** Influence of time step size for the G&R homeostatic model

inhomogeneous concentrated stress field; this could cause some numerical difficulty in the computation of healing by coupling the numerical approximation in both spatial and time domains.

5.2.3 Non-local Comellas model

Similarly, the response obtained with the *non-local Comellas model* is shown in Figs. 10, 11 and 12c. The average stress curves and the distribution of damage fields $f(d)$ show that there is no mesh dependence, and the non-local approach has permitted to overcome the mesh dependence which was reported in Comellas et al. (2016). Similar

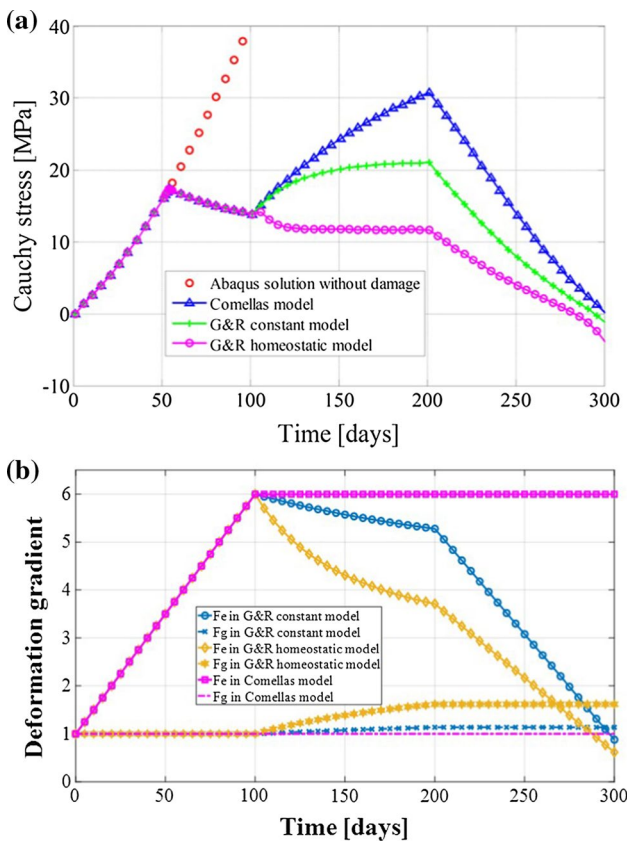


Fig. 3 Comparison of G&R constant model, the *G&R homeostatic model* and the non-local Comellas model. **a** Stress–time curves; **b** temporal variations of the deformation gradient

results as for the G&R healing models are found for the Comellas model by using different c_d values, as shown in Fig. 11.

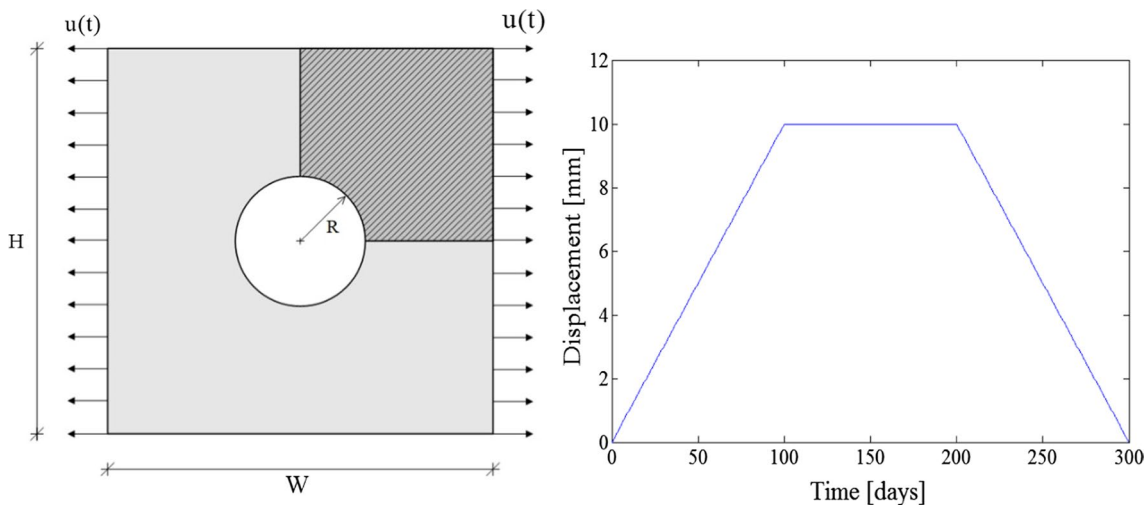


Fig. 4 Geometry and displacement applied for the open-hole rectangular plate case study

5.3 Balloon angioplasty case study

The third case study is related to damage induced by balloon angioplasty and its healing for a long-time scale. The two-dimensional geometry shown in Fig. 13a was previously established by Badel et al. (2014), inspired from histological pictures of epicardial coronary arteries from Viles-Gonzalez et al. (2011). The coronary artery is assumed to consist of a single medial layer containing an atherosclerotic plaque, and the balloon used for angioplasty is modeled as a thin circular structure whose diameter increases during the angioplasty process. The medial layer and the plaque are modeled based on a neo-Hookean hyperelastic model, and the balloon is modeled with a linear elastic model. The geometry and the FEM mesh are shown in Fig. 13b, and the material parameters are reported in Table 4.

The only boundary conditions to be assigned are the nodal displacements of the balloon. A radial displacement is imposed to each node from its initial position, $d_i = 0.5$ mm, to give a final deformed diameter, $d_f = 1$ mm. In the following, we use variable $\lambda = (d - d_i) / (d_f - d_i)$, where d is the current diameter of the balloon, as a gauge of the inflation progress. The balloon inflation is applied from time $t = 0$ to $t = 100$ days, and the healing is set to begin from time $t = 100$ days and the boundary condition is set as constant. Note that all the degrees of freedom of the balloon are prescribed as Dirichlet boundary conditions. Therefore, the response of the balloon is completely independent of the material behavior assigned to it, so we assigned a linear elastic model for the balloon.

The process from damage to healing is simulated during balloon angioplasty for the same three models as in previous sections. The final deformation of balloon is set as $d_f = 1$ mm for all three models. The results are shown

Table 3 Hyperelastic, damage and healing parameters used in the open-hole tensile test example

Type	Description	Symbol	Values	Units
Hyperelastic	Shear modulus	μ_e	0.1	MPa
	Bulk modulus	κ_e	5.0	MPa
Damage	Saturation parameter	η_d	1.0	MPa ⁻¹
	Damage threshold	κ_d	0.002	MPa
Regularization	Degree of regularization	c_d	0.1, 1.0, 1.0	MPa mm ²
	Penalty parameter	β_d	[0.002, 0.004, 0.006]	MPa
	(Non-)local switch	γ_d	1.0	–
Healing	G&R constant model	k_g	1.0	–
		η_t	–0.001	–
	G&R homeostatic model	k_σ	0.1	–
		η_t	–0.001	–
	Non-local Comellas model	$\dot{\eta}$	0.015	Days ⁻¹
		ξ	0.0	–

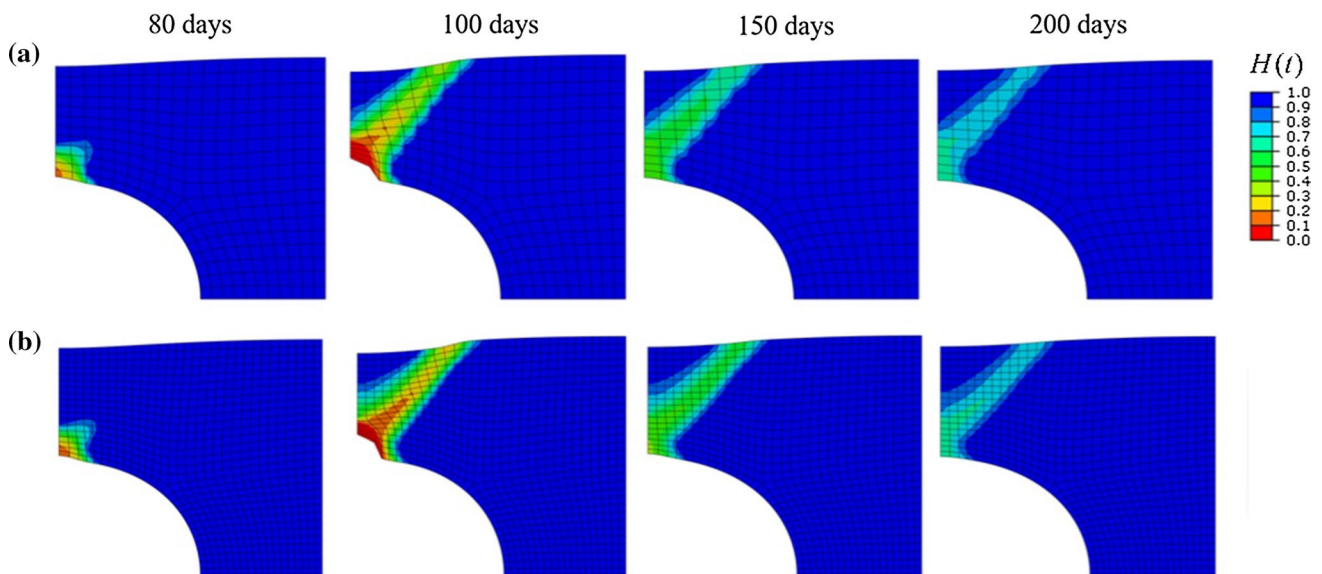


Fig. 5 Evolution of the damage fields throughout the healing process for the non-local G&R constant model. **a** Results with a coarse mesh of 286 elements. **b** Results obtained with a fine mesh of 793 elements

in Fig. 14. All three models successfully simulated medial healing after damage, although the results are slightly different in the distribution of damage fields. Comparatively, the effects of healing are more pronounced for the *G&R constant model* and for the *non-local Comellas model*, but the *G&R homeostatic* shows a more stable process due to the homeostatic condition.

Figure 15 illustrates the effect of different level of balloon inflation setting three different diameters (a) $d_f = 0.9$ mm (b) $d_f = 1.0$ mm and (c) $d_f = 1.1$ mm by using the *G&R constant model*. The first and second columns show two damage fields $H(t)$ in the damage process during the balloon dilation, illustrating that more damage is induced under a larger dilation size. The third and

fourth columns show again the two damage fields $H(t)$ throughout the healing process, in which a recoverable damage can be observed, and an obvious change of geometry of the media layer can be found for case (c) at time $t = 200$ days. This shows the ability of the proposed model in simulating the healing process along with the induced growth deformation.

6 Conclusions

We have developed two new gradient-enhanced continuum healing models for soft tissues, including the gradient-enhanced G&R healing model and the gradient-enhanced

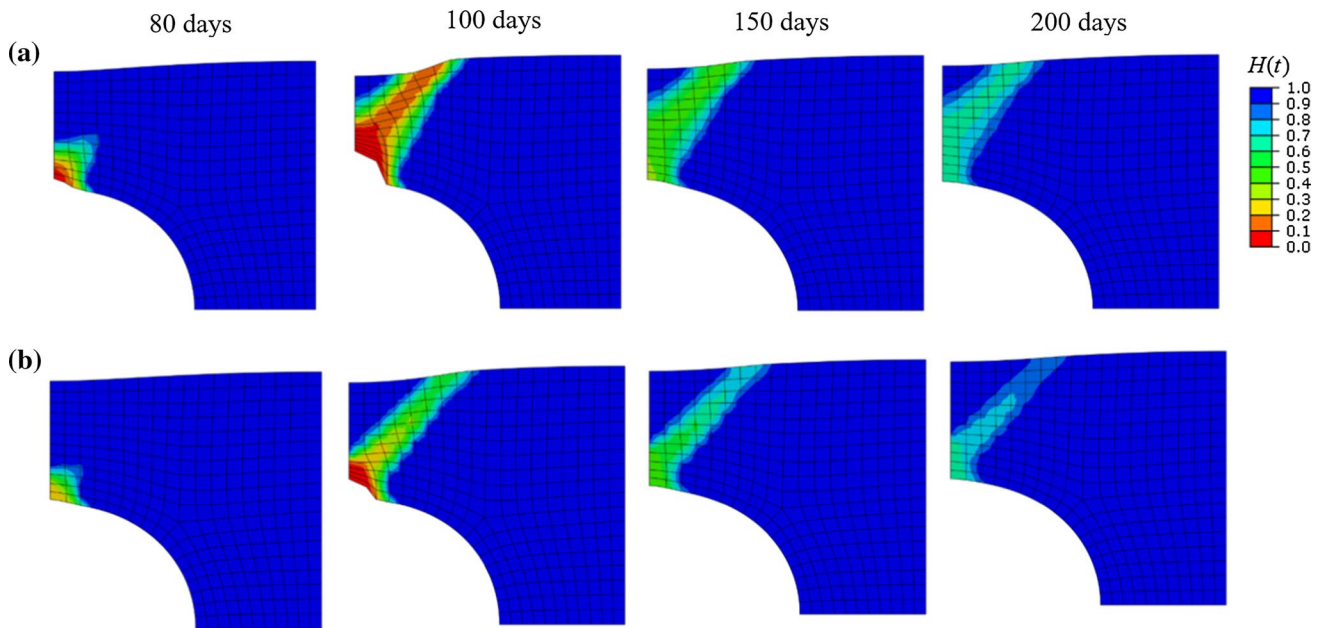


Fig. 6 Evolution of the damage fields throughout the healing process for the non-local G&R constant model. **a** Results with $c_d = 0.1$. **b** Results with $c_d = 10$

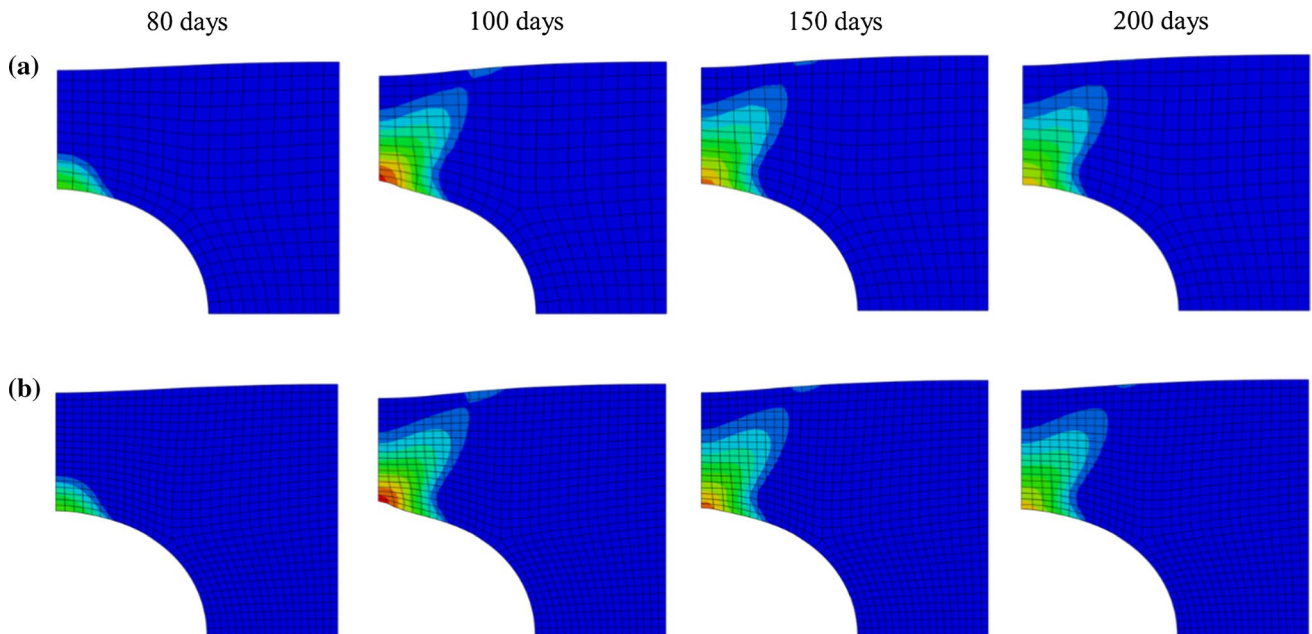


Fig. 7 Evolution of the damage fields throughout the healing process for the non-local *G&R homeostatic model*. **a** Results with a coarse mesh of 286 elements. **b** Results obtained with a fine mesh of 793 elements

version of the healing model proposed by Cormellas et al. (2016) using Abaqus with UEL, and we have shown their potential for applied problems.

A first advantage of the two healing models is their ability to simulate the healing process non-locally by introducing the gradient-enhanced variable. Numerically, a good

mesh independence is achieved in the simulation of healing, even when damage is concentrated in a narrow region.

For the gradient-enhanced G&R healing model, the time-dependent inelastic growth is introduced into the conventional gradient-enhanced damage model to describe the process of G&R in healing in the framework of the temporally

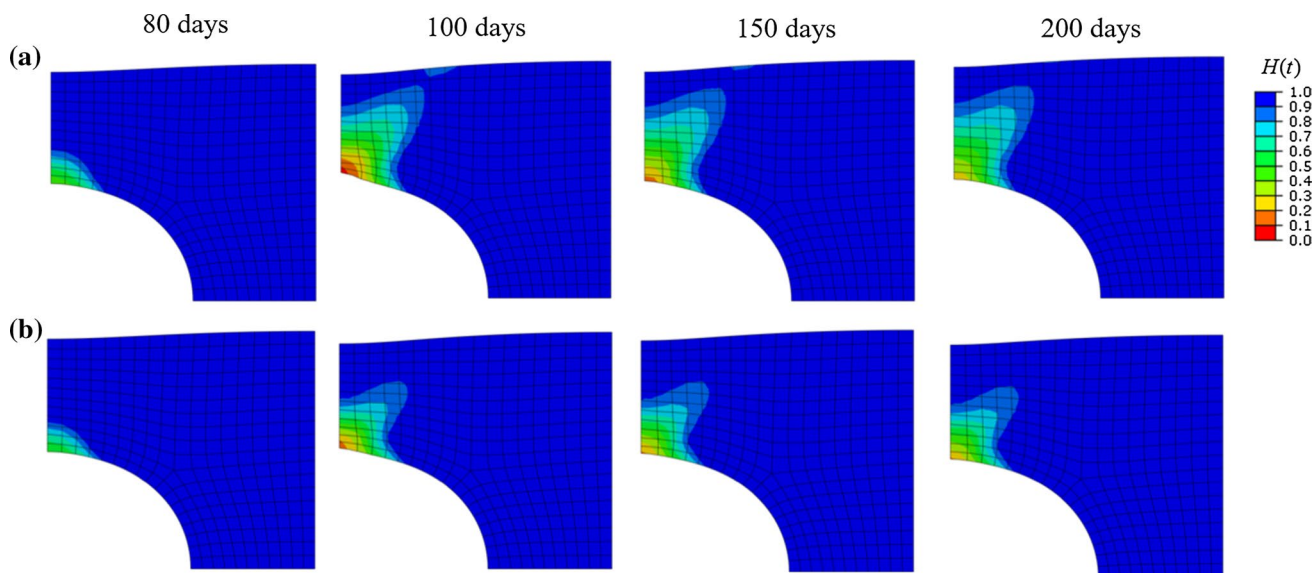


Fig. 8 Evolution of the damage fields throughout the healing process for the non-local *G&R homeostatic model*. **a** Results with $c_d = 1$. **b** Results with $c_d = 10$

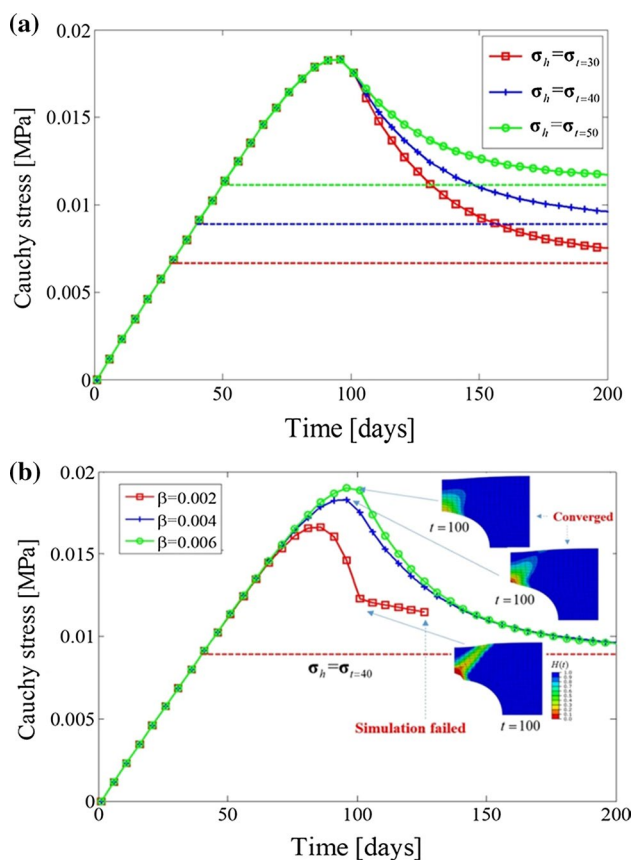


Fig. 9 Evolution of the damage fields throughout the healing process for the non-local *G&R homeostatic model*. **a** Results with different homeostatic stress values. **b** Results with different levels of damage/healing

homogenized growth model (Cyron et al. 2016). In this paper, two approaches to determine the rate of mass production are discussed, including the *G&R constant model* and the *G&R homeostatic model*, and the growth direction is determined according to local principal stress directions. As shown in numerical examples where the effects of the G&R parameters on results are discussed, it seems that the level of damage before the beginning of healing could be a sensitive factor for the convergence toward homeostasis.

Moreover, the difficulty of mesh dependence in original Comellas healing model (Comellas et al. 2016) has been well overcome by virtue of the gradient-enhanced term. Nevertheless, the gradient-enhanced Comellas have not considered the influence of inelastic growth deformation in healing, in comparison with the gradient-enhanced G&R healing models.

Aiming to approach the applied problems, healing after damage in balloon angioplasty is simulated by the proposed models in the last numerical example, and the influence of the inflation diameter on healing is investigated. The proposed models have shown good potential for approaching the healing for damaged soft tissues.

The present model is limited to 2D cases and to isotropic hyperelastic models. However, as collagen fibers are essential in healing of soft tissue, the development of a 3D anisotropic model is currently under progress in order to address more realistic applications. Besides, the use of UEL presents some limitations such as the definition of slave surfaces in contact analyses. Therefore, self-contact problems cannot be addressed with the current model.

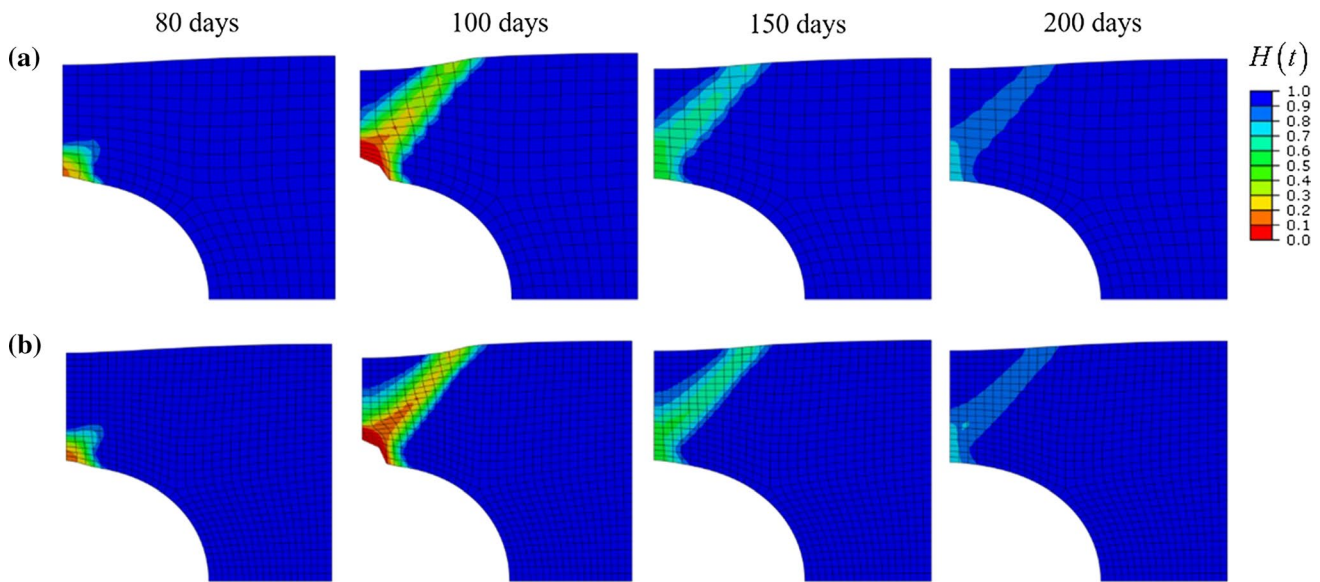


Fig. 10 Evolution of the damage fields throughout the healing process for the non-local Comellas model. **a** Results with a coarse mesh of 286 elements. **b** Results obtained with a fine mesh of 793 elements

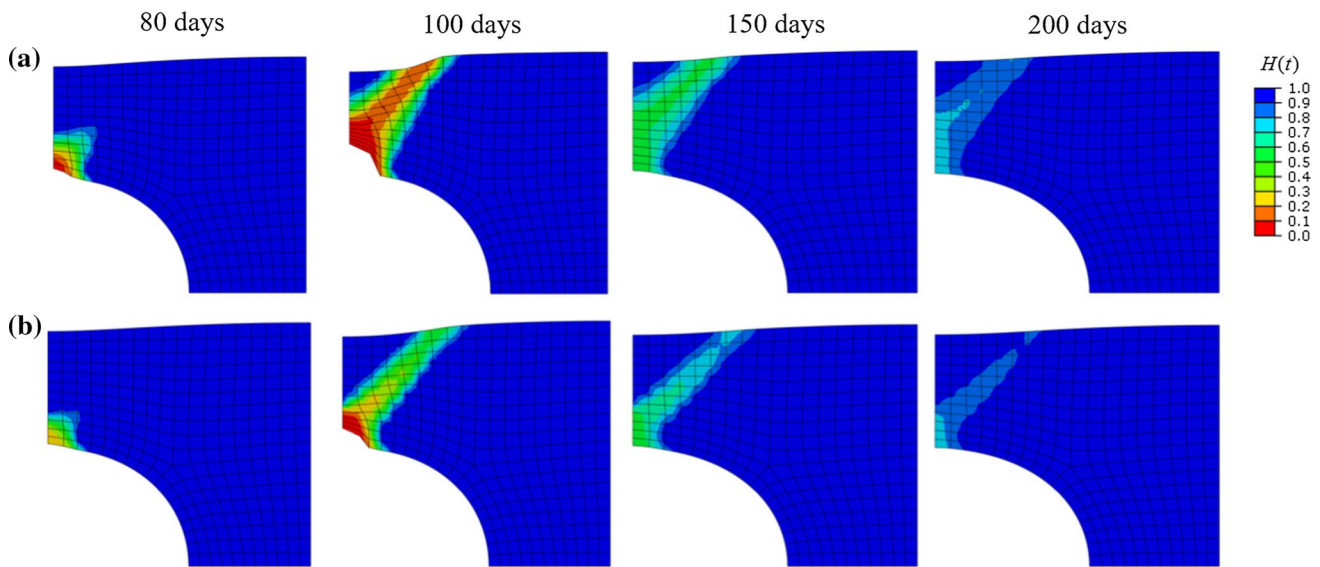


Fig. 11 Evolution of the damage fields throughout the healing process for the non-local Comellas model. **a** Results with $c_d = 1$. **b** Results with $c_d = 10$

The determination of material parameters is also an important issue for the applications of the present model. Generally, hyperelastic parameters can be identified from experimental data and an abundant literature exists on this topic (Avril 2017). But the identification of other parameters, relative for instance to internal length scales, such as the gradient parameter c_d and the penalty parameter β_d will require inverse analyses to be deduced for practical applications

In summary, in this manuscript, two gradient-enhanced constitutive healing models for biological soft tissues including non-local variables have been presented. Important developments are currently under progress for considering the anisotropic constitutive and extension to 3D for more practical applications. The development of a 3D anisotropic model will permit simulating arterial healing after surgical procedures such as angioplasty and stent deployment. This will require defining realistic geometries

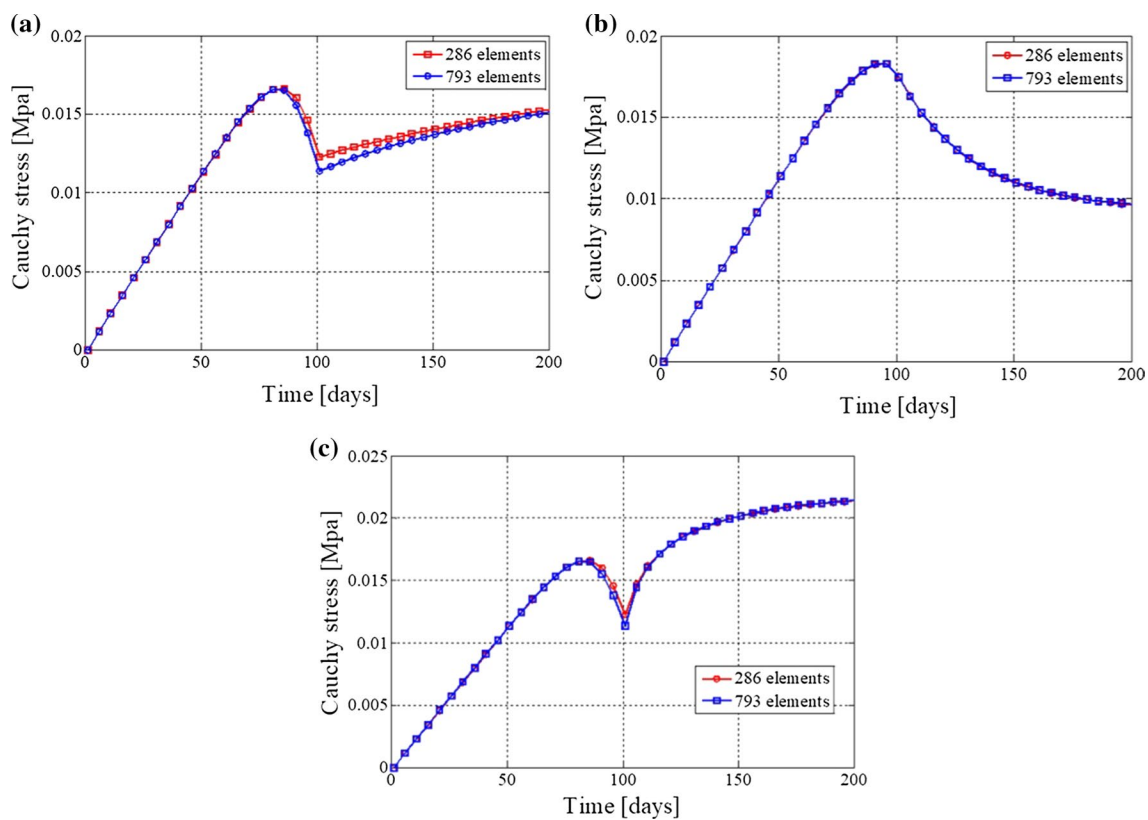


Fig. 12 Plate with a hole. Average Cauchy stress curves for 286 and 793 elements of three different non-local models. **a** G&R constant model, **b** G&R homeostatic model and **c** Comellas model

Fig. 13 a Reference model: geometry, dimensions and boundary conditions; **b** FEM mesh

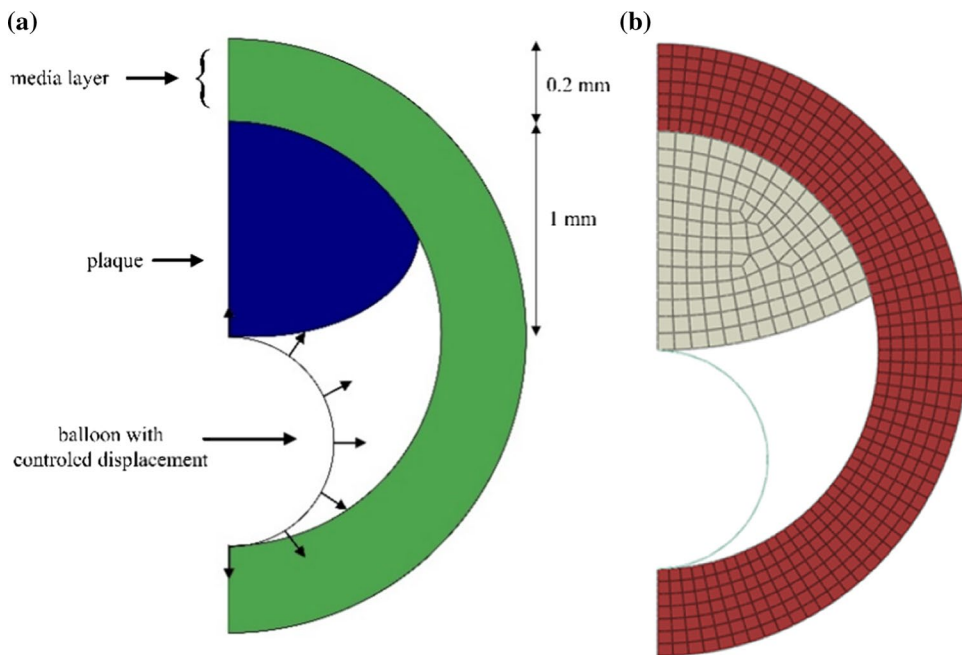


Table 4 Material parameters used in the balloon angioplasty case study (Cyron and Humphrey 2014)

Type	Symbol	Description	Values	Units
<i>Hyperelastic</i>				
Medial layer	μ_e	Shear modulus	200	kPa
	κ_e	Bulk modulus	2.0	MPa
Plaque	μ_p	Shear modulus	20	kPa
	κ_p	Bulk modulus	34	kPa
Balloon	μ_b	Shear modulus	0.5	MPa
	κ_b	Bulk modulus	2.0	MPa
<i>Damage</i>				
Medial layer	η_d	Saturation parameter	1.0	MPa ⁻¹
	κ_d	Damage threshold	5.0	kPa
<i>Regularization</i>				
Medial layer	c_d	Degree of regularization	1.0	MPa mm ²
	β_d	Penalty parameter	5.0	kPa
	γ_d	(Non-)local switch	1.0	–
<i>Healing</i>				
G&R constant model	k_g	Gain parameter	1.0	–
	η_t	Survive function parameter	-0.001	–
G&R homeostatic model	k_σ	Gain parameter	0.05	–
Non-local Comellas model	$\dot{\eta}$	Healing rate	0.015	Days ⁻¹
	ξ	Un-recover percentage	0	–

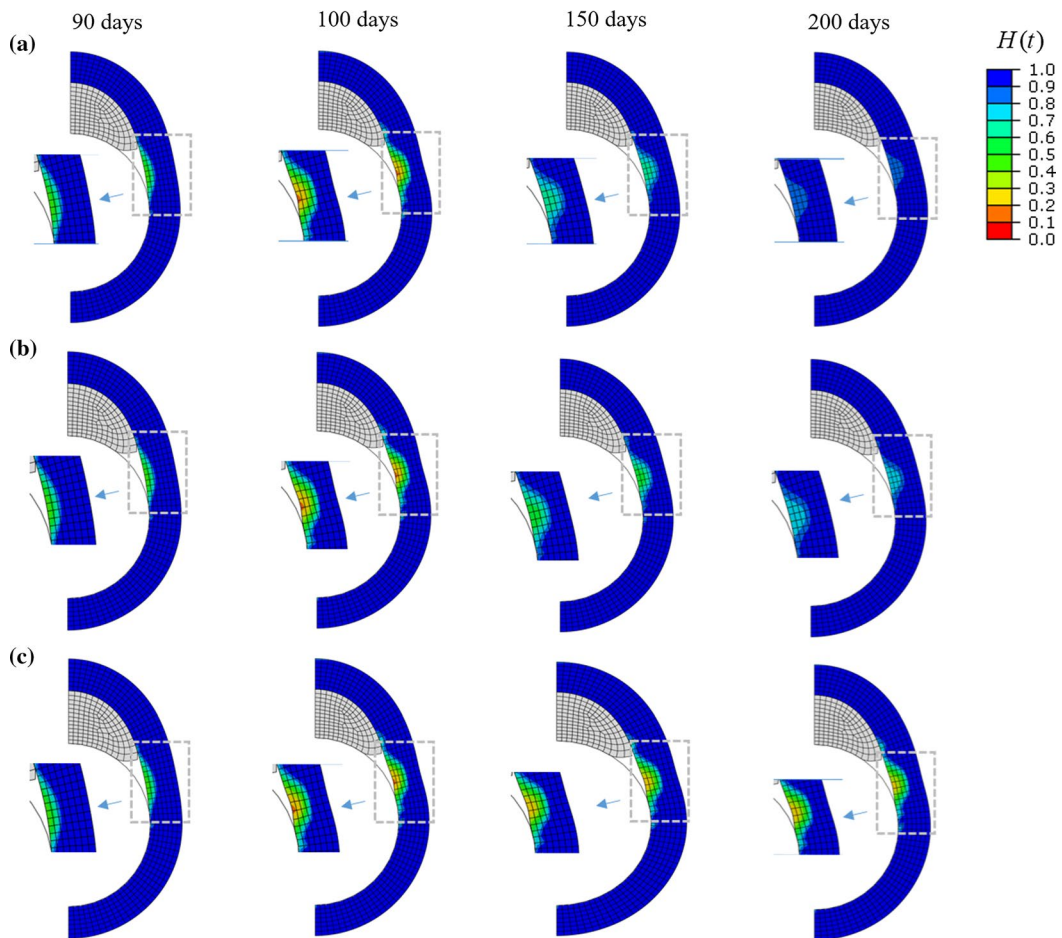


Fig. 14 Evolution of the damage fields throughout the healing process for three different non-local models. **a** Comellas model, **b** G&R constant model and **c** G&R homeostatic model

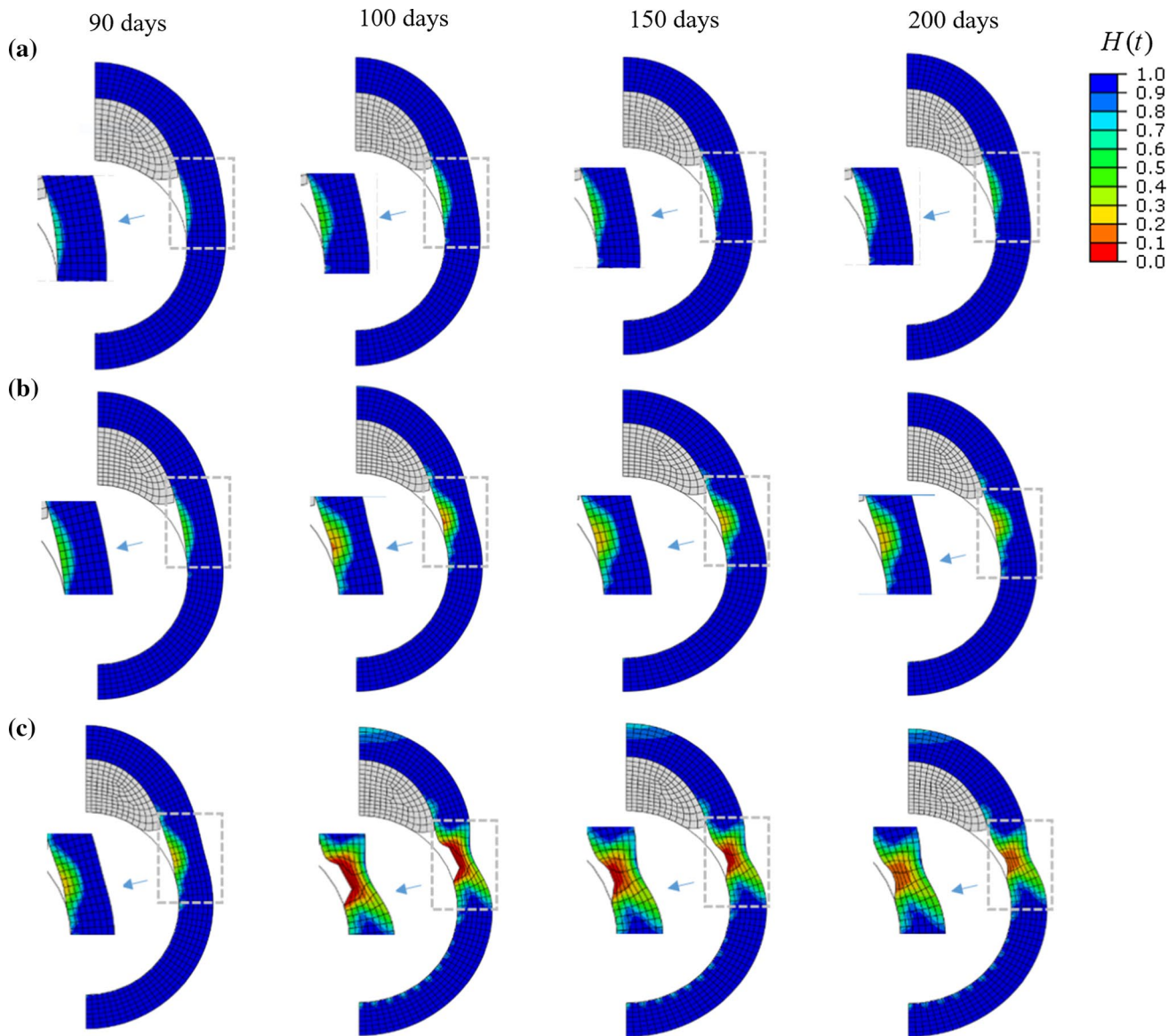


Fig. 15 Evolution of the damage fields throughout the healing process for three different inflation diameters. **a** $d_f = 0.9$ mm, **b** $d_f = 1.0$ mm and **c** $d_f = 1.1$ mm

and appropriate constitutive models to be able to predict the long-term adaptation of arteries to these invasive procedures. Available information about the microstructure of concerned arteries will permit defining the internal length scales.

Acknowledgements The research leading to this paper is funded by ERC-2014-CoG-BIOLOCHANICS [647067], NSFC-ERC Grant [11711530644], NSFC Grant [11572077] and Open Fund from the State Key Laboratory of Structural Analysis for Industrial Equipment [GZ1708]. The authors also acknowledge the support from Prof. Pierre Badel for the model of balloon angioplasty.

References

- Avril S (2017) Hyperelasticity of soft tissues and related inverse problems. In: Avril S, Evans S (eds) Material parameter identification and inverse problems in soft tissue biomechanics, Springer, Berlin, pp 37–66
- Badel P, Avril S, Sutton MA, Lessner SM (2014) Numerical simulation of arterial dissection during balloon angioplasty of atherosclerotic coronary arteries. *J Biomech* 47(4):878–889
- Braeu FA, Seitz A, Aydin RC, Cryon CJ (2017) Homogenized constrained mixture models for anisotropic volumetric growth and remodeling. *Biomech Model Mechanobiol* 16(3):1–18
- Comellas E, Gasser TC, Bellomo FJ, Oller S (2016) A homeostatic-driven turnover remodelling constitutive model for healing in soft tissues. *J R Soc Interface* 13(116):20151081

- Cumming BD, Mcelwain DLS, Upton Z (2009) A mathematical model of wound healing and subsequent scarring. *J R Soc Interface* 7(42):19–34
- Cyron CJ, Humphrey JD (2014) Vascular homeostasis and the concept of mechanobiological stability. *Int J Eng Sci* 85:203–223
- Cyron CJ, Humphrey JD (2017) Growth and remodeling of load-bearing biological soft tissues. *Meccanica* 52(3):645–664
- Cyron CJ, Aydin RC, Humphrey JD (2016) A homogenized constrained mixture (and mechanical analog) model for growth and remodeling of soft tissue. *Biomech Model Mechanobiol* 15(6):1–15
- Davis HG (1867) *Conservative surgery*. Appleton, New York
- Dimitrijevic BJ, Hackl K (2008) A method for gradient enhancement of continuum damage models. *Tech Mech* 1(28):43–52
- Dimitrijevic BJ, Hackl K (2011) A regularization framework for damage–plasticity models via gradient enhancement of the free energy. *Int J Numer Methods Biomed Eng* 27:1199–1210
- Famaey N, Vastmans J, Fehervary H, Maes L, Vanderveken E, Rega F, Mousavi SJ, Avril S (2018) Numerical simulation of arterial remodeling in pulmonary autografts. *Z Angew Math Mech* 98:2239–2257
- Fernández JR, García-Aznar JM, Martínez R (2012) Numerical analysis of a diffusive strain-adaptive bone remodelling theory. *Int J Solids Struct* 49:2085–2093
- Ferreira JPS, Parente MPL, Jabareen M et al (2017) A general framework for the numerical implementation of anisotropic hyperelastic material models including non-local damage. *Biomech Model Mechanobiol* 16(4):1119–1140
- Ganghoffer J-F (2010a) Eshelby tensors, thermodynamics and calculus of variations. Application to volumetric growth. *Int J Eng Sci* 48(12):2081–2098
- Ganghoffer Jean-François (2010b) Mechanical modeling of growth considering domain variation—part II: volumetric and surface growth involving Eshelby tensors. *J Mech Phys Solids* 58(9):1434–1459
- Ganghoffer J-F (2012) Extremum principles for biological continuous bodies undergoing volumetric and surface growth. *Bull Pol Acad Sci Tech Sci* 60(2):259–263
- Ganghoffer JF, Boubaker MB (2017) Micromechanical analysis of volumetric growth in the context of open systems thermodynamics and configurational mechanics. *Contin Mech Thermodyn* 29(2):429–455
- Ganghoffer J-F, Haussy B (2005) Mechanical modeling of growth considering domain variation. Part I: constitutive framework. *Int J Solids Struct* 42(15):4311–4337
- Humphrey JD, Rajagopal KR (2011) A constrained mixture model for growth and remodeling of soft tissues. *Math Models Methods Appl Sci* 12(03):407–430
- Humphrey JD, Dufresne ER, Schwartz MA (2014) Mechanotransduction and extracellular matrix homeostasis. *Nat Rev Mol Cell Biol* 15(12):802–812
- Javierre E, Moreo P, Doblaré M, García-Aznar JM (2009) Numerical modeling of a mechano-chemical theory for wound contraction analysis. *Int J Solids Struct* 46(20):3597–3606
- Menzel A (2005) Modelling of anisotropic growth in biological tissues: a new approach and computational aspects. *Biomechan Model Mechanobiol* 3:147–171
- Mousavi SJ, Farzaneh S, Avril S (2018) Computational predictions of damage propagation preceding dissection of ascending thoracic aortic aneurysms. *Int J Numer Methods Biomed Eng*. <https://doi.org/10.1002/cnm.2944>
- Rodriguez EK, Hoger A, McCulloch AD (1994) Stress-dependent finite growth in soft elastic tissues. *J Biomech* 27(4):455–467
- Sáez P, Peña E, Martínez MA, Kuhl E (2014) Computational modeling of hypertensive growth in the human carotid artery. *Comput Mech* 53(6):1183–1196
- Schugart RC, Friedman A, Zhao R, Sen CK (2008) Wound angiogenesis as a function of tissue oxygen tension: a mathematical model. *Proc Natl Acad Sci U S A* 105(7):2628
- Simo JC, Ju JW (1987) Strain- and stress-based continuum damage models—I. *Formul Int J Solids Struct* 12(3):821–840
- Tepole AB, Kuhl E (2013) Systems-based approaches toward wound healing. *Pediatr Res* 73(2):553–563
- Valentin A, Holzapfel GA (2012) Constrained mixture models as tools for testing competing hypotheses in arterial biomechanics: a brief survey. *Mech Res Commun* 42:126–133
- Valentín A, Humphrey JD, Holzapfel GA (2013) A finite element-based constrained mixture implementation for arterial growth, remodeling, and adaptation: theory and numerical verification. *Int J Numer Methods Biomed Eng* 29(8):822–849
- Valero C, Javierre E, Menzel A (2015a) Challenges in the modeling of wound healing mechanisms in soft biological tissues. *Ann Biomed Eng* 43(7):1654–1665
- Valero C, Javierre E, García-Aznar JM, Gómez-Benito MJ, Menzel A (2015b) Modeling of anisotropic wound healing. *J Mech Phys Solids* 79:80–91
- Viles-Gonzalez JF, De CMR, Scanavacca M, Sosa E, D’Avila A (2011) Acute and chronic effects of epicardial radiofrequency applications delivered on epicardial coronary arteries. *Circ Arrhythm Electrophysiol* 4(4):526
- Waffenschmidt T, Polindara C, Menzel A, Blanco S (2014) A gradient-enhanced large-deformation continuum damage model for fibre-reinforced materials. *Comput Methods Appl Mech Eng* 268(1):801–842

Publisher’s Note Springer Nature remains neutral with regard to jurisdictional claims in published maps and institutional affiliations.